Automatic Mediastinal Lymph Node Detection in Chest CT

Marco Feuerstein[a], Daisuke Deguchi[b], Takayuki Kitasaka[b,c], Shingo Iwano[d],
Kazuyoshi Imaizumi[b,d], Yoshinori Hasegawa[b,d], Yasuhito Suenaga[a,b], Kensaku Mori[a,b]

[a]Graduate School of Information Science, Nagoya University, Japan;
[b]MEXT Innovation Center for Preventive Medical Engineering, Nagoya University, Japan;
[c]Faculty of Management and Information Science, Aichi Institute of Technology, Japan;
[d]Graduate School of Medicine, Nagoya University, Japan

ABSTRACT

Computed tomography (CT) of the chest is a very common staging investigation for the assessment of mediastinal, hilar, and intrapulmonary lymph nodes in the context of lung cancer. In the current clinical workflow, the detection and assessment of lymph nodes is usually performed manually, which can be error-prone and time-consuming. We therefore propose a method for the automatic detection of mediastinal, hilar, and intrapulmonary lymph node candidates in contrast-enhanced chest CT. Based on the segmentation of important mediastinal anatomy (bronchial tree, aortic arch) and making use of anatomical knowledge, we utilize Hessian eigenvalues to detect lymph node candidates. As lymph nodes can be characterized as blob-like structures of varying size and shape within a specific intensity interval, we can utilize these characteristics to reduce the number of false positive candidates significantly. We applied our method to 5 cases suspected to have lung cancer. The processing time of our algorithm did not exceed 6 minutes, and we achieved an average sensitivity of 82.1% and an average precision of 13.3%.

Keywords: Lung, Other Organs, CAD Development, Segmentation, Classification

1. INTRODUCTION

Computed tomography (CT) of the chest is the most common means of staging the mediastinum in patients with lung cancer. Despite not being the exclusive means, it remains the first choice between supplementary staging methods such as positron emission tomography, bronchoscopy, needle aspiration, and endoscopic ultrasound.[1] The evaluation of the mediastinum for the detection and assessment of lymph node metastasis or lymphoma is not only highly important for staging, but also for the prediction of surgical resectability and the support of treatment and therapy.

In the current clinical workflow of lung cancer staging, radiologists and other physicians have to detect, quantitatively evaluate, and classify lymph nodes in one of the 14 hilar, intrapulmonary, and mediastinal lymph node stations,[2] which is done manually by examining all slices of (usually contrast-enhanced) CT datasets of the chest. This process can be very time-consuming, and lymph nodes may be overlooked easily, in particular by novice physicians. To overcome these problems, we propose a method to automatically detect mediastinal, hilar, and intrapulmonary lymph node candidates.

While approaches for the segmentation of lymph nodes in CT images based on a few mouse clicks or more interaction[3–6] and for the automatic assignment of regional lymph node stations[7, 8] have been proposed previously, little work has been done on the automatic detection of lymph nodes. To our knowledge, so far only three approaches[9–11] to (semi-)automatic lymph node detection in CT datasets were presented. Before Eicke[9] could start an automatic extraction process of neck lymph nodes by template matching in the Fourier space, he manually adjusted the lymph node intensity (HU) range for each experimental dataset by means of a previously obtained gold standard segmentation. Kitasaka et al.[10] do not require a manual initialization of their automatic lymph node detection algorithm. However, along with a runtime of about two to three hours per CT dataset, the

---

resulting true positive rate (TPR) was only 57%. A recent method proposed by Dornheim and Dornheim[11] uses stable mass spring models to automatically find enlarged neck lymph nodes of size greater than 8 mm. Though very promising, their technique was only evaluated on one dataset. Furthermore, while other groups focus on neck and abdominal lymph nodes, we target the mediastinum, which is a region highly affected by cardiac and breathing motion (leading to imaging artifacts) and thus more difficult to process than the neck or abdomen.

2. METHOD

In order to design a pipeline for automatic lymph node detection, we first try to identify the features of (mediastinal, hilar, and intrapulmonary) lymph nodes. We can describe the nodes to generally be of ellipsoidal shape. However, in many cases they tend to be "banana-shaped". Furthermore, lymph nodes can be of various sizes. Whereas healthy lymph nodes vary between 1 and 20 mm in diameter (along their longitudinal axis assuming ellipsoidal shape),[12] benign and malignant ones can grow up to about 5 to 35 mm.[13] In any case, they often touch or infiltrate nearby vessels and soft tissue, which can additionally alter their shape. These characteristics make a clear definition of our search space very difficult. We could only identify one feature common to all lymph nodes: to some extent, they are all blobs containing voxels of a particular intensity interval. A second feature common to mediastinal, hilar, and intrapulmonary lymph nodes is (by definition) their location. They are close or adjacent to the bronchial tree, upper aortic arch, esophagus, and pulmonary ligament.[2]

Based on these features, we designed our algorithm for the automatic detection of mediastinal, hilar, and intrapulmonary lymph nodes in contrast-enhanced chest CT datasets. First, we extract the anatomical structures defining the location of the lymph nodes[*] (cf. Sec. 2.1 and 2.2). Next, we extract vessels and bony structures in the mediastinum to restrict the search space of lymph nodes (cf. Sec. 2.3). Finally, Hessian analysis is performed to enhance blob-like structures (cf. Sec. 2.4), followed by a series of steps to reduce the number of false positive detections (cf. Sec. 2.5).

2.1 Bronchial tree segmentation

To extract the bronchial tree, we first estimate the minimum bounding box of the lung. This can be done automatically, since the lung is the organ containing most air and, thus, its CT contains mainly low intensities. Within the lung region, we perform a region growing based bronchial tree extraction. In order to start the region growing algorithm, we automatically determine a seed point in an axial slice of the upper part of the lung by analyzing the circularity of air regions. Finally, by comparing the size and number of segmented bronchial tree regions in axial direction, the bifurcation of the trachea into left and right main bronchus is determined.

Alternatively, we could also employ more sophisticated approaches for bronchial tree segmentation,[14–17] but for our case a bifurcation of up to about the fourth branching level is enough, as most mediastinal, hilar, and intrapulmonary lymph nodes appear around the trachea, main bronchi, lobar bronchi, segmental bronchi, and large subsegmental bronchi.

2.2 Upper aortic arch segmentation

The upper end of the aortic arch lies above the bifurcation of the trachea. This anatomical knowledge allows us to efficiently and robustly search for a seed point for aortic arch segmentation. Considering a sub-volume around the bifurcation only, we search for Hough circles in equidistant axial slices 15 to 25 mm below the bifurcation. Based on region growing using a sphere of 8 mm radius for voxels above the threshold 70 HU (Hounsfield units), we first determine the top slice still containing the aortic arch and from there extract the upper part (60 mm) of the aortic arch in axial direction.

---

[*]Note that the esophagus and pulmonary ligament are currently not extracted, as paraesophageal and pulmonary ligament lymph nodes are not very likely. In our experimental datasets, a radiologist could only identify a single pulmonary ligament lymph node out of all 106 lymph nodes.

2.3 Vessel and bone extraction

Using the same seed point and threshold as for the aortic arch, we automatically segment an outline of vessels and bones. Running consecutive region growing algorithms with spheres of 8, 7, 6, 5, 4, 3, and 2 mm radius, we analyze the volume sizes of regions newly added by each consecutive grow. If a volume size is too small (less than a sphere of 20 mm in radius), we can assume the corresponding region to be a wrongly detected lymph node and subtract it from the segmentation results. Otherwise, it will very likely be a vessel, which is usually rather constant in radius and, assuming it to be long enough, larger in volume than a lymph node, or a bone, which generally has a larger volume than a lymph node.

2.4 Hessian analysis

Dilating the segmented bronchial tree and the upper aortic arch by a sphere of 20 mm in radius and subtracting the original regions from the dilation results, we can define our search region for mediastinal, hilar, and intrapulmonary lymph nodes. Within the minimum bounding box of this search region, we determine the Hessian matrix

$$H(f)_\sigma = \begin{bmatrix} \frac{\partial^2 f}{\partial x^2} & \frac{\partial^2 f}{\partial x \partial y} & \frac{\partial^2 f}{\partial x \partial z} \\ \frac{\partial^2 f}{\partial y \partial x} & \frac{\partial^2 f}{\partial y^2} & \frac{\partial^2 f}{\partial y \partial z} \\ \frac{\partial^2 f}{\partial z \partial x} & \frac{\partial^2 f}{\partial z \partial y} & \frac{\partial^2 f}{\partial z^2} \end{bmatrix} \tag{1}$$

for each voxel x, y, z of intensity $f(x, y, z)$ by convolution with the second and cross derivatives of a Gaussian[18] of scale σ. Using a QL decomposition, we receive its corresponding eigenvalues $\lambda_1, \lambda_2, \lambda_3$ ($|\lambda_1| \leq |\lambda_2| \leq |\lambda_3|$). For each voxel, we compute a "blobness" response measure[19–21] $B(\lambda)_\sigma$:

$$B(\lambda)_\sigma = \begin{cases} 255 \cdot \left(1 - e^{-\frac{R_A^2}{2\alpha^2}}\right) \cdot \left(1 - e^{-\frac{S^2}{2\gamma^2}}\right) & \text{if } \lambda_j < 0 \text{ for } j = 1 \ldots 3 \\ 0 & \text{otherwise} \end{cases} \tag{2}$$

with

$$R_A = \frac{|\lambda_2|}{|\lambda_3|} \tag{3}$$

and

$$S = \sqrt{\lambda_1^2 + \lambda_2^2 + \lambda_3^2} \tag{4}$$

$B(\lambda)_\sigma$ is defined between 0 and 255 and gives high responses for $\lambda_1 \approx \lambda_2 \approx \lambda_3$. The smaller the eigenvalues, the higher is $B(\lambda)_\sigma$. Equally weighting $\alpha = \gamma = 1$ in equation 2 gave the best empirically determined compromise between a low number of true positives and a high number of false positives. $B(\lambda)_\sigma$ is computed for the scales $\sigma = 1.5$, 2.5, and 3.5 (mm). We selected these scales, as our experiments showed that lower scales resulted in many additional small blobs (not being lymph nodes) and adding higher scales gives no further information, but much longer runtime. Finally, the maximum response $B(\lambda)$ is selected for each voxel:

$$B(\lambda) = \max_{\sigma \in \{1.5, 2.5, 3.5\}} B(\lambda)_\sigma \tag{5}$$

Each lymph node candidate is represented by a blob consisting of 6-connected voxels featuring a blobness measure of at least 1.

2.5 False positive reduction

As the Hessian eigenvalue analysis gives us many false positive lymph node candidates, we reduce this high number in 4 steps (see Fig. 1):

1. We first threshold our original image (not the blobness response image) to only contain voxels inside the intensity interval [-15, 170] HU and inside our search region adjacent to the upper aortic arch and bronchial tree. On this thresholded image, we perform a morphological opening using a sphere of 1.5 mm radius in order to remove small vessels, which are adjacent to a lymph node, and to eliminate any other non-spherical structures.
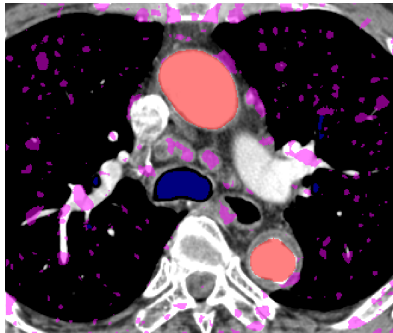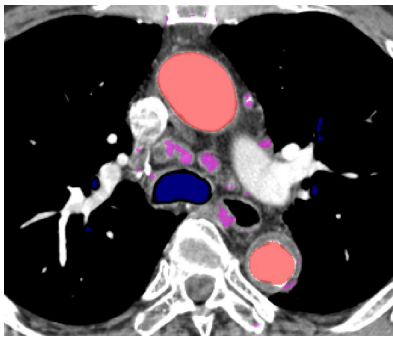
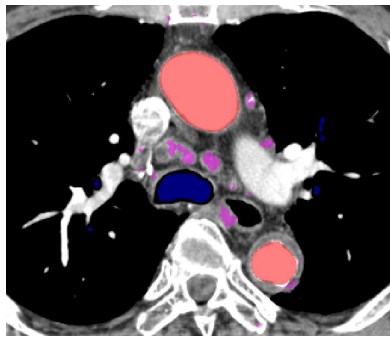(a) Initial blobness response after Hessian analysis
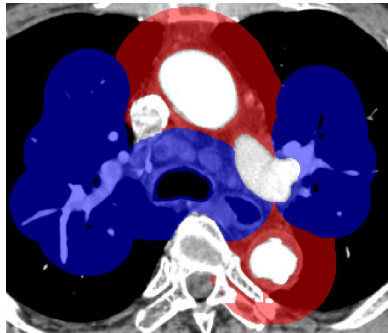
(b) Search region
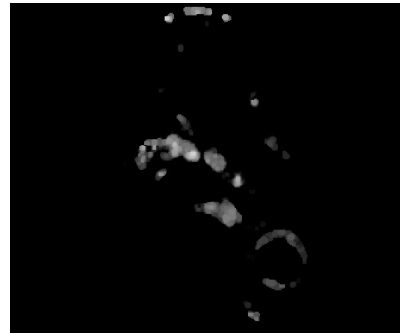
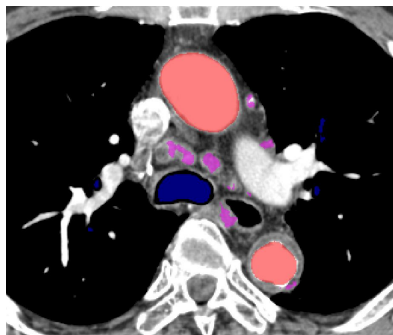(c) Morphological opening on thresholded original image

(d) Reduction step 1: Removal of blobs outside search region (b) and opened image (c)
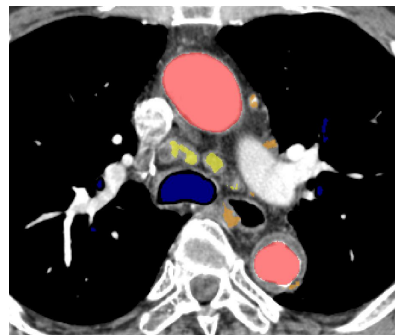
(e) Reduction step 2: Removal of small blobs

(f) Reduction step 3: Extended 3-D Min-DD filter

(g) Reduction step 4: Removal of blobs not exceeding a specific blobness measure threshold

(h) True positive (yellow) versus false positive (orange) lymph nodes

Figure 1: False positive reduction steps depicted for slice 153 of case 3, where lymph node candidates are colored pink, the upper aortic arch red, and the bronchial tree blue.

2. We remove blobs, which are smaller than $(1.5 \text{ mm})^3$.

3. We apply the extended 3-D Min-DD filter[10] to all voxels of candidate blobs (after median filtering the image):

$$h(x, y, z)_r = \min_{\theta_1, \theta_2, \phi_1, \phi_2} 2f(x, y, z) - \{f(x + r\cos(\theta_1)\cos(\theta_2), y + r\sin(\theta_1), z + r\cos(\theta_1)\sin(\theta_2)) +$$

$$f(x - r\cos(\theta_1 + \phi_1)\cos(\theta_2 + \phi_2), y - r\sin(\theta_1 + \phi_1), z - r\cos(\theta_1 + \phi_1)\sin(\theta_2 + \phi_2))\} \quad (6)$$

with $0 \le \theta_1 \le 2\pi$, $0 \le \theta_2 \le 2\pi$, $-\frac{\pi}{2} \le \phi_1 \le \frac{\pi}{2}$, and $-\frac{\pi}{2} \le \phi_2 \le \frac{\pi}{2}$ (setting a step size of $\frac{\pi}{8}$). For each voxel, the extended 3-D Min-DD filter generates evenly distributed sample points on a sphere centered at the voxel[†] and for each sample another set of points laying on a hemisphere opposite the sample. Then it compares the intensities of the voxel with the sample points and their corresponding points on the hemispheres. If the intensity of the voxel is higher than the intensities of all sample points, the filter will give a positive response. We apply the filter to multiple scales using radii r of $1.5, 2.0, 2.5, \ldots, 8.0$ mm, and determine the maximum response:

$$h(x, y, z) = \max_{r \in \{1.5, 2.0, 2.5, \ldots, 8.0\}} h(x, y, z)_r \quad (7)$$

Blobs not containing any filtered voxels greater than 5 are removed.

4. We remove blobs not containing any voxels with blobness measure greater than an empirically determined threshold. A response measure of 30 gave good results in our experiments.

3. RESULTS AND DISCUSSION

From 5 contrast-enhanced chest CT datasets (with acquisition parameters stated in Table 1), together with a radiologist we manually obtained gold standard segmentations of all mediastinal, hilar, and intrapulmonary lymph nodes[‡] with minimum, average, and maximum diameter of 1.5, 10.6, and 39.7 mm, respectively. We implemented our proposed method using MIST[§] and ITK[¶] and applied it to the 5 datasets on a workstation with two 64-bit Quad-Core Intel Xeon 5355 processors and 8GB main memory.

Table 1: Scan acquisition parameters. The first 2 cases were acquired by a Toshiba Aquilion scanner, the latter 3 by a General Electrics Discovery scanner.

Case	Slices	Voxel Spacing	Voltage	Current
1	687	$(0.625\text{mm})^2 \times 0.5\text{mm}$	135kV	300mA
2	813	$(0.665\text{mm})^2 \times 0.5\text{mm}$	135kV	300mA
3	310	$(0.586\text{mm})^2 \times 1.0\text{mm}$	140kV	300mA
4	271	$(0.586\text{mm})^2 \times 1.0\text{mm}$	140kV	380mA
5	266	$(0.625\text{mm})^2 \times 1.0\text{mm}$	140kV	379mA

We estimated the processing time and the number of true positive (TP), false negative (FN), and false positive (FP) candidates, from which in turn we obtained the true positive rate (TPR, sensitivity) and positive predictive value (PPV, precision). The results of our method are summarized in Table 2 and Fig. 2.

We also analyzed the true positive rates and positive predictive values for each false positive reduction step, as summarized in Table 3. After the second step, 88.7% of all lymph nodes could be successfully detected, while

---

[†]The sample points on the sphere are defined by θ_1 and θ_2 and distributed by geodesic subdivision. For our step size of $\frac{\pi}{8}$ we get 66 sample points.

[‡]Two of the 106 segmented lymph nodes actually were supraclavicular and not mediastinal, hilar, or intrapulmonary.

[§]Media Integration Standard Toolkit – `http://mist.suenaga.m.is.nagoya-u.ac.jp/trac-en/`

[¶]National Library of Medicine Insight Segmentation and Registration Toolkit – `http://www.itk.org/`

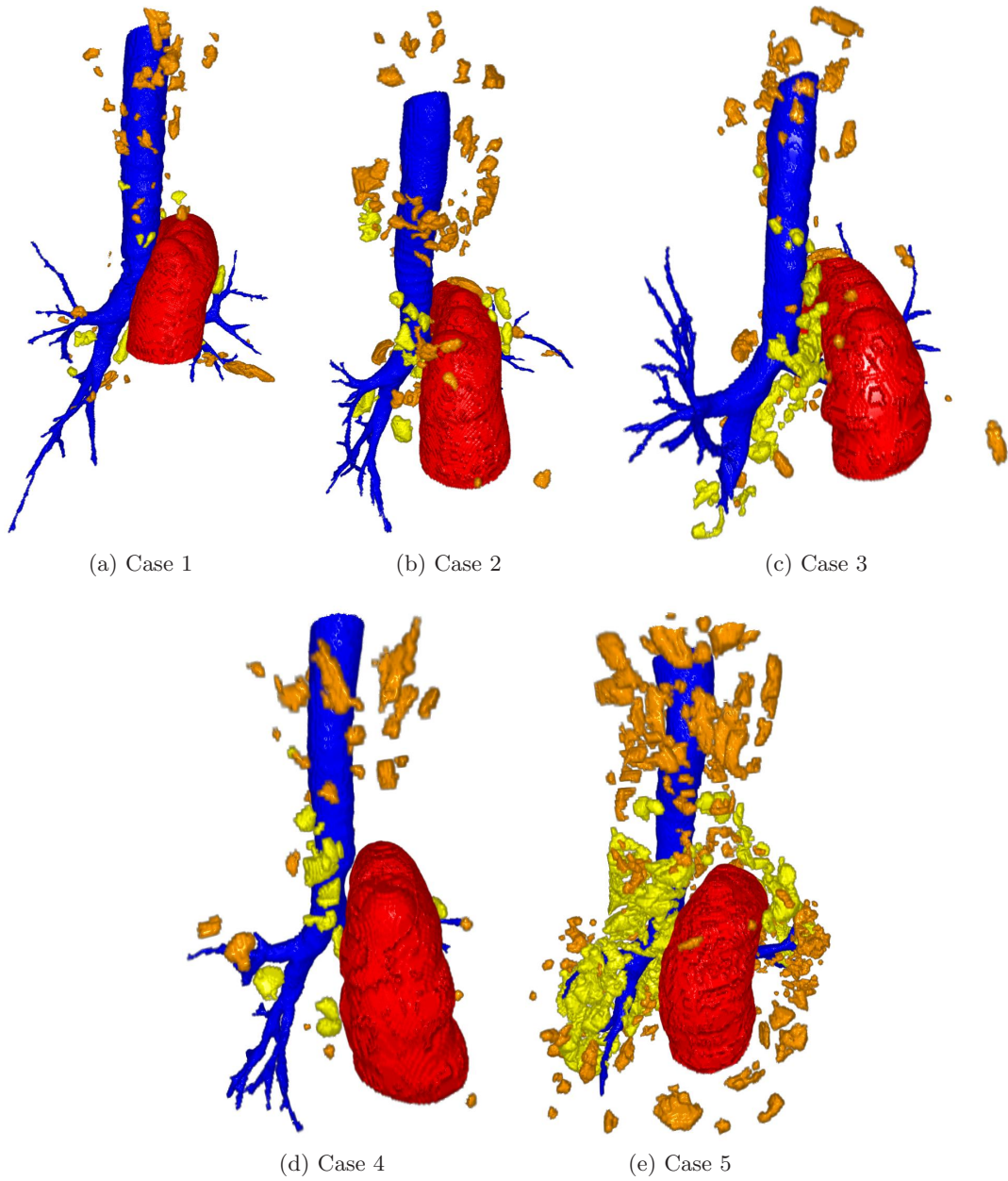(a) Case 1 (b) Case 2 (c) Case 3

(d) Case 4 (e) Case 5

Figure 2: Exemplary lymph node map generated for all 5 cases shown as volume rendering. The bronchial tree is colored blue, the upper aortic arch red, and lymph node candidates are highlighted yellow in case of true positives and orange in case of false positives.

Table 2: Detection results after all 4 steps to reduce false positives.

Case	TP	FN	FP	TPR	PPV	Time
1	14	8	72	63.3%	16.3%	5:15 min
2	21	5	93	80.8%	18.4%	5:19 min
3	16	2	84	88.9%	16.0%	2:52 min
4	10	2	45	83.3%	18.2%	1:55 min
5	26	2	273	92.9%	8.7%	3:35 min
Total	87	19	567	82.1%	13.3%	

about 1 out of 13 candidates was a real lymph node. After the fourth step, we still detected 82.1% lymph nodes, while already 1 out of 8 candidates was a lymph node.

Table 3: False positive reduction steps. 0 corresponds to the results after Hessian analysis, 1 to 4 to the 4 consecutive steps.

Step	TP	FN	FP	TPR	PPV
0	103	3	27073	97.2%	0.4%
1	94	12	2785	88.7%	3.3%
2	94	12	1126	88.7%	7.7%
3	89	17	691	84.0%	11.4%
4	87	19	567	82.1%	13.3%

Looking at the detection results (see Fig. 3), we could identify many false positive lymph nodes inside the esophagus and the non-contrast-enhanced part of the heart. In our future work we will therefore also incorporate segmentations of these anatomical structures into our processing pipeline. Furthermore, we need to enhance our vessel and bone segmentation process, in particular for smaller and low-contrast ones, which were not entirely extracted and sometimes wrongly detected as lymph node candidates. A few times we also wrongly detected muscles as lymph nodes, which needs to be tackled in the future. For case 5 we obtained a rather low PPV (8.7%). This can be due to the fact that the patient, who is suspected to suffer from severe lymphoma, had a very high number of enlarged lymph nodes. We may have not been able to include all of these lymph nodes into our gold standard segmentation as they were often not easily identifiable and distinguishable from other soft tissue or lymph nodes. Further investigation is needed.

Some of our candidate lymph nodes only cover a small portion of the real node. This may be addressed in the future by incorporating one of the seed point based segmentation techniques into our method.

Table 4 shows a comparison of our method to the state-of-the-art in automatic lymph node detection. Contrary to Eicke[9] our method is fully automatic, and features similar TPR (sensitivity) and higher PPV (precision). Compared to Kitasaka et al.[10] our precision is lower. We however anticipate a great improvement, once we include a segmentation of esophagus and heart into our processing pipeline and improve our current vessel and bone segmentation method. Furthermore, our work features a much higher sensitivity and processing time. The results of Dornheim and Dornheim[11] are very promising too, but are not yet thoroughly evaluated on multiple datasets and only detect nodes greater than 8 mm. In comparison, we can also detect smaller benign and malignant nodes as well as healthy nodes greater than 1.5 mm.

4. CONCLUSIONS

This work for the first time presents a speedy and automatic segmentation pipeline for the detection of mediastinal, hilar, and intrapulmonary lymph nodes with high sensitivity and adequate precision. In the order of minutes, we are able to generate a map of lymph node candidates to support the assessment needs of physicians.
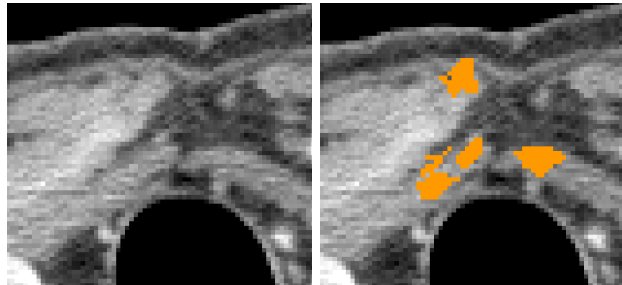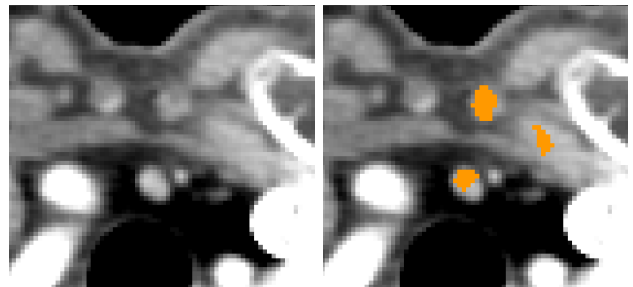
(a) False positives inside infrahyoid muscles (bottom) and jugular vein (top)
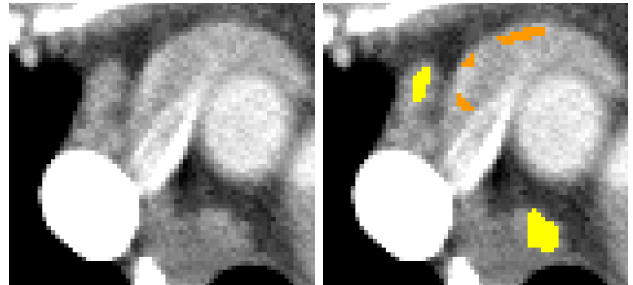
(b) False positives inside left brachiocephalic vein, and true positive highest mediastinal (left) and retrotracheal nodes (bottom right)
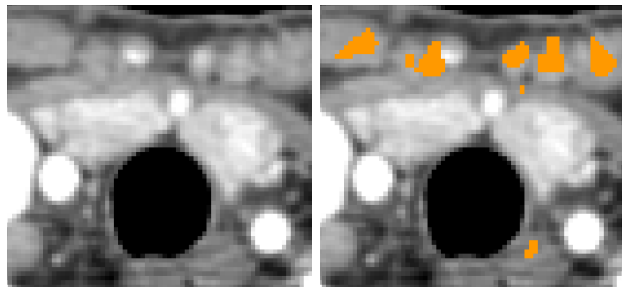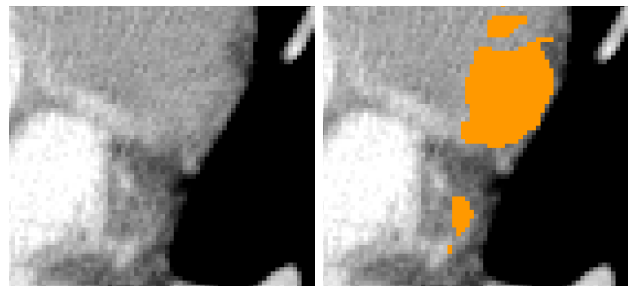

(c) False positives inside jugular veins (top middle), sternocleidomastoid muscle (top left and top right), and esophagus (bottom)
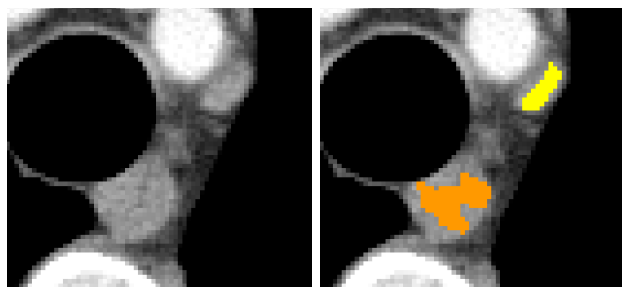

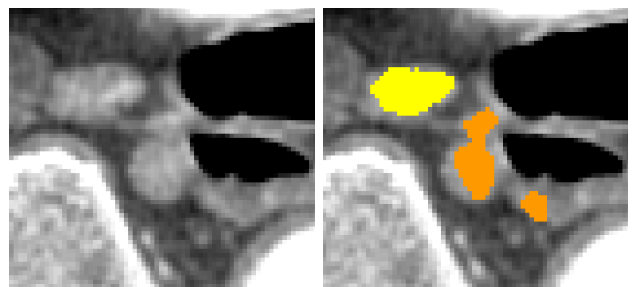(d) False positives inside sternohyoid muscle (top), inferior thyroid vein (bottom), and other tissue (right)
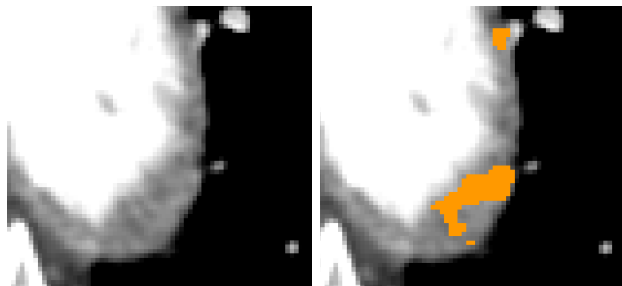
(e) False positives inside the non-contrasted part of the aortic arch

(f) False positives inside the non-contrasted part of the heart

(g) False positive node inside the upper esophagus and true positive highest mediastinal node

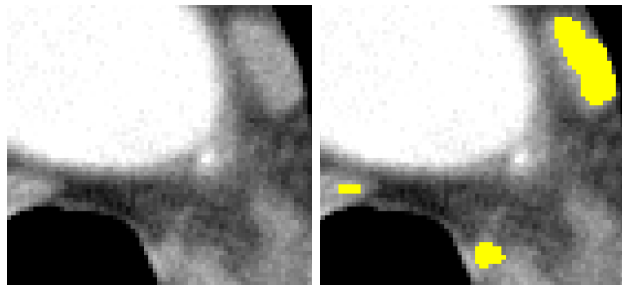(h) False positives adjacent to the middle esophagus and true positive hilar node

Figure 3: Exemplary lymph node candidates. In each subfigure, the original CT image is shown on the left (window level: 30 HU, window width: 400 HU) and overlaid with extracted lymph nodes on the right. False positive candidates are colored orange, true positives yellow.
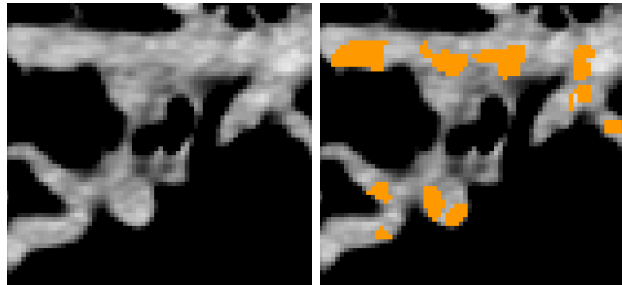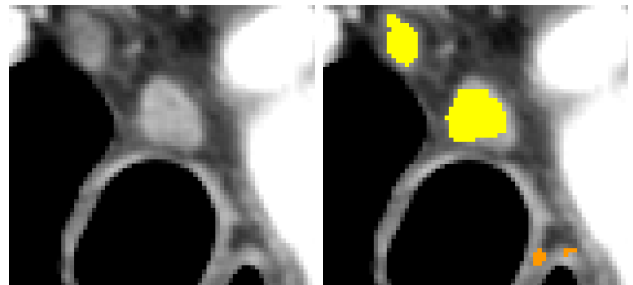
(i) False positives in the right pulmonary vein – case 5 with suspected severe lymphoma
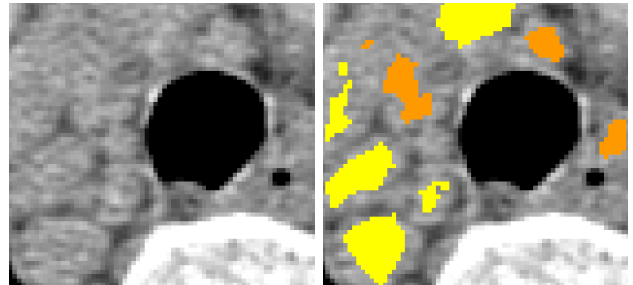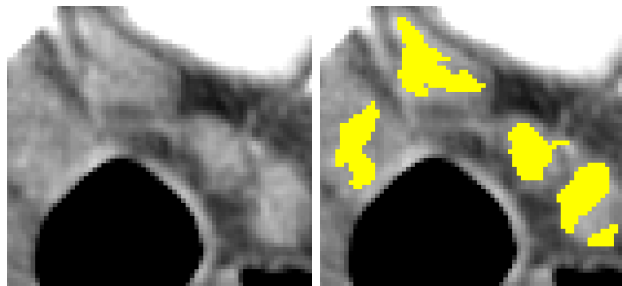
(j) True positive highest mediastinal nodes – case 5 with suspected severe lymphoma
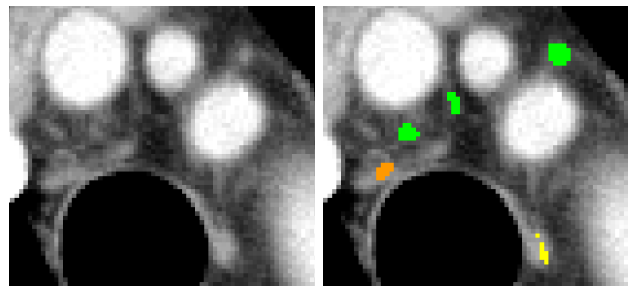
(k) True positive retrotracheal node (left), lower paratracheal node (bottom), and para-aortic node (upper right)

(l) True positive upper paratracheal nodes and false positives adjacent to esophagus

(m) True positive upper paratracheal node (top middle) and retrotracheal nodes (left and right)

(n) False negative nodes (middle: retrotracheal, top right: upper paratracheal) rejected due to their small size, true positive retrotracheal node (left), and false positive upper paratracheal node (bottom)
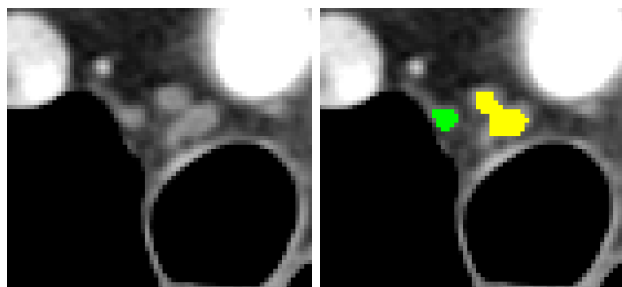
(o) False negative (rejected due to its small size) and true positive highest mediastinal nodes
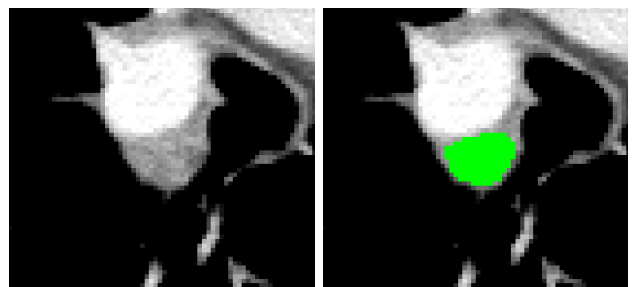
(p) False negative lobar node close to the right pulmonary artery

Figure 3: Exemplary lymph node candidates and missed nodes. In each subfigure, the original CT image is shown on the left (window level: 30 HU, window width: 400 HU) and overlaid with extracted or missed lymph nodes on the right. False positive candidates are colored orange, true positives yellow, and false negatives green.

Table 4: Comparison of our method to current state-of-the-art methods

Method	Target Area	Cases	Size of Nodes	Fully Automatic	TPR	PPV	Time
Eicke[9]	Neck	3	> 5.0 mm	no	87.0%	5.9%	unknown
Kitasaka[10]	Abdomen	5	> 5.0 mm	yes	57.0%	30.3%	approx. 2-3 h
Dornheim[11]	Neck	1	> 8.0 mm	yes[a]	100.0%	76.3%	approx. 17 min[b]
Ours	Mediastinum	5	> 1.5 mm	yes	82.1%	13.3%	1-6 min

[a] after initial definition of search region

[b] excluding time for search region generation

The availability of an automatic lymph node detection technique will not only support physicians, but also enhance all previously proposed interactive segmentation methods.[3–6] Seed points required to start the segmentation process could be automatically selected from the output of our method and, once the segmentation is automated, assignment methods for regional lymph node stations can be further automated.[7,8] Eventually this will establish a more sophisticated computer aided diagnosis of lung cancer.

We believe that our method is a first but important step towards aiding physicians in an error-prone, laborious, and time-consuming cancer staging process.

ACKNOWLEDGMENTS

REFERENCES

[1] Sihoe, A. D. L. and Yim, A. P. C., "Lung cancer staging," *Journal of Surgical Research* **117**, 92–106 (2004).

[2] Mountain, C. F. and Dresler, C. M., "Regional lymph node classification for lung cancer staging," *Chest* **111**, 1718–1723 (1997).

[3] Yan, J., Zhuang, T.-g., Zhao, B., and Schwartz, L. H., "Lymph node segmentation from ct images using fast marching method," *Computerized Medical Imaging and Graphics* **28**, 33–38 (January 2004).

[4] Dornheim, J., Seim, H., Preim, B., Hertel, I., and Strauss, G., "Segmentation of neck lymph nodes in ct datasets with stable 3d mass-spring models: Segmentation of neck lymph nodes," *Academic Radiology* **14**, 1389–1399 (2007).

[5] Lu, K. and Higgins, W. E., "Interactive segmentation based on the live wire for 3d ct chest image analysis," *International Journal of Computer Assisted Radiology and Surgery* **2**, 151–167 (December 2007).

[6] Jolly, M.-P. and Grady, L., "3d general lesion segmentation in ct," in [*ISBI*], 796–799, IEEE (2008).

[7] Kiraly, A. P., Naidich, D. P., Guendel, L., Zhang, L., and Novak, C. L., "Novel method and applications for labeling and identifying lymph nodes," in [*Medical Imaging 2007: Physiology, Function, and Structure from Medical Images*], Manduca, A. and Hu, X. P., eds., *Proc. of SPIE* **6511** (March 2007).

[8] Lu, K., Merritt, S. A., and Higgins, W. E., "Extraction and visualization of the central chest lymph-node stations," in [*Medical Imaging 2008: Computer-Aided Diagnosis*], Giger, M. L. and Karssemeijer, N., eds., *Proc. of SPIE* **6915** (March 2008).

[9] Eicke, D., *Detektion von Lymphknoten in Hals CT-Datensätzen*, Master's thesis, Otto-von-Guericke-Universität Magdeburg (2005).

[10] Kitasaka, T., Tsujimura, Y., Nakamura, Y., Mori, K., Suenaga, Y., Ito, M., and Nawano, S., "Automated extraction of lymph nodes from 3-d abdominal ct images using 3-d minimum directional difference filter," in [*MICCAI*], Ayache, N., Ourselin, S., and Maeder, A., eds., *LNCS 4792*(Part II), 336–343, Springer-Verlag (2007).

[11] Dornheim, L. and Dornheim, J., "Automatische Detektion von Lymphknoten in CT-Datensätzen des Halses," in [*Workshop - Bildverarbeitung für die Medizin (BVM)*], (2008).

[12] Genereux, G. P. and Howie, J. L., "Normal mediastinal lymph node size and number: Ct and anatomic study," *American Journal of Roentgenology* **142**(6), 1095–1100 (1984).

[13] Arita, T., Matsumoto, T., Kuramitsu, T., Kawamura, M., Matsunaga, N., Sugi, K., and Esato, K., "Is it possible to differentiate malignant mediastinal nodes from benign nodes by size?," *Chest* **110**, 1004–1008 (1996).

[14] Kitasaka, T., Mori, K., Suenaga, Y., ichi Hasegawa, J., and ichiro Toriwaki, J., "A method for segmenting bronchial trees from 3d chest x-ray ct images," in [*MICCAI*], Ellis, R. and Peters, T., eds., *LNCS* **2879**, 603–610 (2003).

[15] Tschirren, J., Hoffman, E. A., McLennan, G., and Sonka, M., "Intrathoracic airway trees: Segmentation and airway morphology analysis from low-dose ct scans," *IEEE Transactions on Medical Imaging* **24**, 1529–1539 (December 2005).

[16] Graham, M. W., Gibbs, J. D., and Higgins, W. E., "Robust system for human airway-tree segmentation," in [*Medical Imaging 2008: Image Processing*], Reinhardt, J. M. and Pluim, J. P. W., eds., *Proc. of SPIE* **6914** (March 2008).

[17] Lo, P. and de Bruijne, M., "Voxel classification based airway tree segmentation," in [*Medical Imaging 2008: Image Processing*], Reinhardt, J. M. and Pluim, J. P. W., eds., *Proc. of SPIE* **6914** (March 2008).

[18] Farnebäck, G. and Westin, C.-F., "Improving deriche-style recursive gaussian filters," *Journal of Mathematical Imaging and Vision* **26**, 293–299 (December 2006).

[19] Frangi, A. F., Niessen, W. J., Vincken, K. L., and Viergever, M. A., "Multiscale vessel enhancement filtering," in [*MICCAI*], *LNCS* **1496**, 130–137 (1998).

[20] Sato, Y., Westin, C.-F., Bhalerao, A., Nakajima, S., Shiraga, N., Tamura, S., and Kikinis, R., "Tissue classification based on 3d local intensity structures for volume rendering," *IEEE Transactions on Visualization and Computer Graphics* **6**, 160–180 (April–June 2000).

[21] Antiga, L., "Generalizing vesselness with respect to dimensionality and shape," *The Insight Journal* (July–December 2007).